Optical Materials 76 (2018) 407–415

Contents lists available at ScienceDirect

Optical Materials

journal homepage: www.elsevier.com/locate/optmat

Tunable green/red luminescence by infrared upconversion in biocompatible forsterite nanoparticles with high erbium doping uptake

Rúbia Young Sun Zampiva [a, *], Luiz Henrique Acauan [b], Janio Venturini [a], Jose Augusto Martins Garcia [c, d], Diego Silverio da Silva [e], Zhaohong Han [f], Luciana Reyes Pires Kassab [f], Niklaus Ursus Wetter [e], Anuradha Agarwal [f], Annelise Kopp Alves [a], Carlos Pérez Bergmann [a]

[a] Department of Materials Engineering, Federal University of Rio Grande do Sul- UFRGS. Osvaldo Aranha 99, Porto Alegre, RS, 90035- 190, Brazil
[b] Department of Aeronautics and Astronautics, Massachusetts Institute of Technology-MIT, Cambridge, MA, 02139, United States
[c] Laboratório de Tecnologia em Materiais Fotônicos e Optoeletrônicos, Faculdade de Tecnologia de São Paulo, Praça Coronel Fernando Prestes, 30 - Bom Retiro, São Paulo, SP, 01124-060, Brazil
[d] Laboratório de Sistemas Integráveis, Escola Politécnica da Universidade de São Paulo, Av. Prof. Luciano Gualberto, 158, Travessa 3, 05508-900, São Paulo, SP, Brazil
[e] Centro de Lasers e Aplicações, Instituto de Pesquisas Energéticas e Nucleares-IPEN/SP, Prof. Lineu Prestes 2242, São Paulo, SP, 05508-000, Brazil
[f] Microphotonics Center, Massachusetts Institute of Technology-MIT, Cambridge, MA, 02139, United States

ARTICLE INFO

Article history:
Received 13 November 2017
Received in revised form
13 December 2017
Accepted 4 January 2018

Keywords:
Biomaterial
Erbium doping
Forsterite nanoparticles
Tunable emission
Upconversion

ABSTRACT

Nanoparticles represent a promising platform for diagnostics and therapy of human diseases. For biomedical applications, these nanoparticles are usually coated with photosensitizers regularly activated in a spectral window of 530–700 nm. The emissions at 530 nm (green) and 660 nm (red) are of particular interest for imaging and photodynamic therapy, respectively. This work presents the $Mg_2SiO_4:Er^{3+}$ system, produced by reverse strike co-precipitation, with up to 10% dopant and no secondary phase formation. These nanoparticles when excited at 985 nm show upconversion emission with peaks around 530 and 660 nm, although excitation at 808 nm leads to only a single emission peak at around 530 nm. The direct upconversion of this biomaterial without a co-dopant, and its tunability by the excitation source, renders $Mg_2SiO_4:Er^{3+}$ nanoparticles a promising system for biomedical applications.

© 2018 Elsevier B.V. All rights reserved.

1. Introduction

In the recent past, rare earth doped nanoparticles rose as a topic of growing interest due to their distinct optical properties [1]. Crystalline structures doped with rare earth ions exhibit well-defined absorption and emission lines and do not undergo photobleaching [2,3], making these nanoparticles extremely advantageous for biomedical applications. In crystalline nanoparticles, the absorber and emitter ions inside the structure are shielded from the outside environment, thus there is little or no quenching related to the biological medium in which it they are inserted [4–7].

For biomedical applications, these nanoparticles are usually coated with photosensitizers activated in a spectral window of 530–700 nm [6,8,9] and the location of light exposure is controlled; it is therefore possible to target specific cells, such as bacterial cells or tumors. The emissions around 530 nm (green) and 660 nm (red) are of particular interest for imaging and photodynamic therapy (PDT) [6,8,9], as they also activate a variety of anticancer drugs [10–15]. However, these wavelengths have reduced tissue penetration, rendering large internal areas virtually inaccessible to diagnosis and treatment purposes. One way to avoid the above-mentioned problem is to shift the excitation wavelength to the near infrared region (NIR). In this spectral region, biological tissues allow high light penetration with minimal absorption, enabling the light to reach targets in deep positions inside living organisms [8,16]. Therefore, NIR excitation sources can be used with higher

* Corresponding author.
E-mail address: rubiayoungsun@gmail.com (R.Y.S. Zampiva).

https://doi.org/10.1016/j.optmat.2018.01.004
0925-3467/© 2018 Elsevier B.V. All rights reserved.

intensity and/or exposure time than ultraviolet (UV) and visible (Vis) sources, without causing significant damage to the exposed tissue.

When inserted in specific hosts, rare-earth ions such as Ho^{3+}, Eu^{3+} and Er^{3+} present upconversion emission, i.e. these systems are able to absorb two or more low energy photons and emit at higher energy ranges [17–21]. Recently, upconversion nanoparticles (UCNPs) excited in the NIR have been widely applied in biomedicine. At 800 nm, water and hemoglobin have a minimal NIR absorption and the heating effect is therefore considerably reduced. Overheating may induce cell and tissue damage [4,15,22]. Thus, efforts are being made to adjust the UCNPs excitation window [8,9,23]. Research on platforms based on upconversion is still at an initial state focusing on the manufacturing of nanoparticles. The development of platforms such as UCNPs with tunable emission – particularly the green and red emissions – could represent an important improvement for their application, since with the same system it would be possible to activate different functions by the careful choice of the excitation wavelength [24,25].

The erbium (III) ion presents upconversion when excited at different NIR wavelengths, emitting in the UV–Vis range [10,18,26]. The wavelength and intensity of the absorption and emission lines vary in accordance to the host [27]; in other words, a dopant ion may have distinct optical properties depending on the host in which it is inserted [28]. Forsterite (Mg_2SiO_4) is a biocompatible material with high dielectric constant ($\varepsilon r = \sim 7$) [29,30], elevated transparency in the UV–Vis–NIR range [31] and great physicochemical stability even under extreme conditions ($\geq$1800 °C and a wide range of pH) [29,32,33]. These properties make forsterite an excellent candidate for biological and optical applications. However, it has not yet been extensively studied in the aforementioned fields.

We present for the first time, to the best of our knowledge, the erbium-doped forsterite (Mg_2SiO_4:Er^{3+}) system. Homogeneous nanoparticles of Mg_2SiO_4:Er^{3+} were produced by a low cost technique, namely reverse strike co-precipitation (RSC). This is a simple and effective way to produce large amounts of high quality single-phase nanopowder that are loosely agglomerated [34,35]. Down-conversion and upconversion photoluminescence were measured with excitation at 985 and 808 nm. Interestingly, the produced Mg_2SiO_4:Er^{3+} nanoparticles presented different upconversion emissions depending on the NIR wavelength excitation.

2. Experimental

Nano-scale erbium doped forsterite powder was synthesized via RSC similarly as the pure forsterite powder described by Zampiva at al. [36]. In order to produce Mg_2SiO_4:Er^{3+} (2g), Mg $(NO_3)_2 \cdot 6H2O$ 99% (8.14g), $Si(OC_2H_5)_4$ (TEOS) 98.5% (3.17 mL) and *x* (0%, 1%, 3%, 5%, 7%, 10%, 20% mol) of $Er(NO_3)_3 \cdot 5\ H_2O$99.9% were dissolved in a solution of ethanol (40 mL) and HNO_3 70% (3 mL). All reagents were purchased from Sigma-Aldrich. The reaction follows the stoichiometry described below (Eq. (1)):

$$2\ Mg(NO_3)_2 + Si(OHC_2H_5)_4 + x\ Er(NO_3)_3 \rightarrow Mg_2SiO_4{:}\ Er^{3+} + x\ N_2 + 8\ CO_2 + 12\ H_2O + x\ O_2 \quad (1)$$

The samples crystallinity was evaluated by X-ray diffraction (XRD) using a PHILIPS diffractometer (model X'Pert MPD), 40 kV, 40 mA and Cu anode and the crystallite size was calculated by Scherrer's equation. The specific surface area of the calcined powders were determined by the Brunauer–Emmett–Teller nitrogen gas adsorption method (BET, Micromeritics ASAP2020 gas absorption). Raman spectroscopy was carried out using a Renishaw inVia microRaman System with a 532 nm wavelength laser. X-ray photoelectron spectroscopy (XPS, ESCA 3000-VG Microtech) was performed using Al-Kα radiation for the initial survey as well as for the high resolution measurements. The morphology was characterized by scanning electron microscopy (SEM, JEOL-JSM 6060) at an accelerating voltage between 10 and 20 kV and transmission electron microscopy (TEM, JEM 2010) at 200 kV. The powder samples were dispersed with ethanol, which was dropped onto silicon glass and dried at 60 °C for 2 h. The produced films were then analyzed via absorbance spectroscopy in the UV–Vis–NIR range using an Ocean Optics spectrophotometer. For the emission analyses, the powders were pressed into pellets with a thickness of 1 mm. Photoluminescence measurements were performed in a Micro-PL system (HORIBA Jobin Yvon) with a solid-state laser excitation source (Quantum Laser) operating at 532 nm with 100 mW output power. The emission spectra in the UV–Vis–NIR were obtained by exciting the samples at 808 and 985 nm with an intensity of up to 1 W cm^{-2}; the signals were collected and analyzed by a monochromator equipped with a photomultiplier for signal detection in the visible region (500–700 nm) and with a Ge photodetector for signal detection in the infrared region (1440–1700 nm).

3. Results and discussion

The XRD analysis (Fig. 1) showed that with the variation of erbium concentration in the samples from 0 to 10% mol a single phase of forsterite is observed (synthetic forsterite, PDF# 34-189). In the Mg_2SiO_4: Er^{3+} 20% diffractogram, the presence of magnesium oxide (MgO, PDF # 45-946) is observed, indicating saturation of the host structure and the beginning of competing phase formation. Although structure saturation has occurred, no erbium oxide peaks are observed (Er_2O_3 PDF # 08-0050).

Via Scherrer's calculation, with increasing Er^{3+} concentration in the structure, the crystallites undergo a small gradual growth, ranging from 15 ± 3 nm for the Mg_2SiO_4 sample to 25 ± 2 nm for the Mg_2SiO_4:Er^{3+} 20% sample. Despite the growth of the crystallites, no significant lattice changes were observed according to the XRD analysis. In addition, the surface area analysis by BET, showed

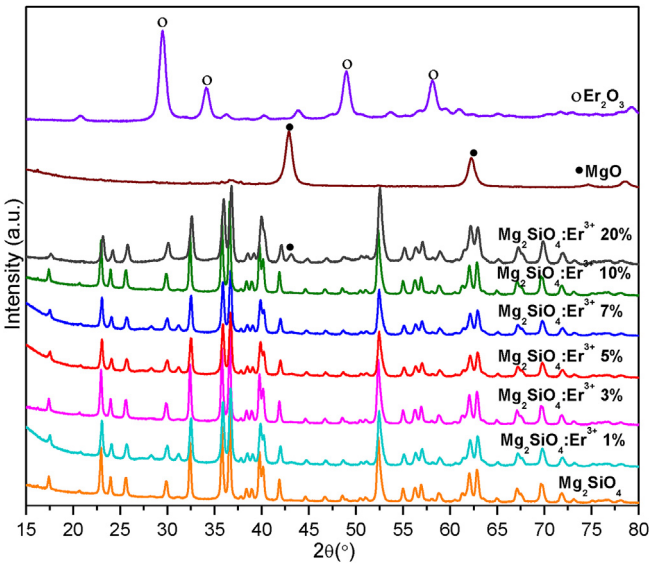


Fig. 1. X-ray diffratograms of commercial MgO, Er_2O_3 and synthesized Mg_2SiO_4 with different Er^{3+} doping concentration. From 0 to 10% a single phase of forsterite is observed. In the Mg_2SiO_4: Er^{3+} 20% diffractogram, the presence of MgO indicates saturation of the host structure.

relatively high surface areas, around 79 ± 2.5 m^2/g, for all these particles. To analyze the Er^{3+} ion influence on the host structure, chemical and morphological analyses were performed at the Mg_2SiO_4:Er^{3+} 10% sample, which presented the highest amount of dopant in the host without secondary phase formation.

Mg_2SiO_4:Er^{3+} 10% TEM analyses show nanoparticles with a mean diameter of 21 nm (Fig. 2a). Furthermore, the [012] lattice plane of Mg_2SiO_4 can be clearly identified (Fig. 2b), indicating that the Er^{3+} insertion in the host (up to 10% mol) did not modify the lattice constant. The same is observed in the electron diffraction pattern (ED) shown in Fig. 2c, which shows several characteristic interplanar spacings of crystalline forsterite.

The conservation of the host crystalline structure observed in the diffractogram (Fig. 1) and complemented by the TEM and ED analyses (Fig. 2) indicate that Er^{3+} ions may occupy substitutional sites in the forsterite crystallite [37,38]. Interestingly, the Mg_2SiO_4:Er^{3+} 20% sample presented MgO as a second phase instead of Er_2O_3, which would be the main product formed by the Er^{3+} that segregated from the host structure. Mg^{2+} in octahedral sites has an ionic radius of around 0.72 Å while Er^{3+} in the same position has an ionic radius of approximately 0.89 Å. These values represent a difference of 19% between the radii of these ions [39,40]. Differences of above 30% in ionic radius do not allow the cations to replace one another, becoming practically impossible to compete for the same site, but when this number is about 15% such a replacement can occur freely [41]. Thus, it is possible for both Mg^{2+} and Er^{3+} ions to occupy the octahedral sites of forsterite. However, the MgO formation as a secondary phase indicates a preferential Er^{3+} occupancy when compared to Mg^{2+} in the octahedral sites.

The elemental distribution in the produced nanoparticles was analyzed via EDS. The compositional mapping from the SEM image (Fig. 3a) shows homogeneous distribution of oxygen, silicon, magnesium, and erbium (Fig. 3b, c, d and e, respectively) in Mg_2SiO_4:Er^{3+} 10% sample, no clusters of any element were found.

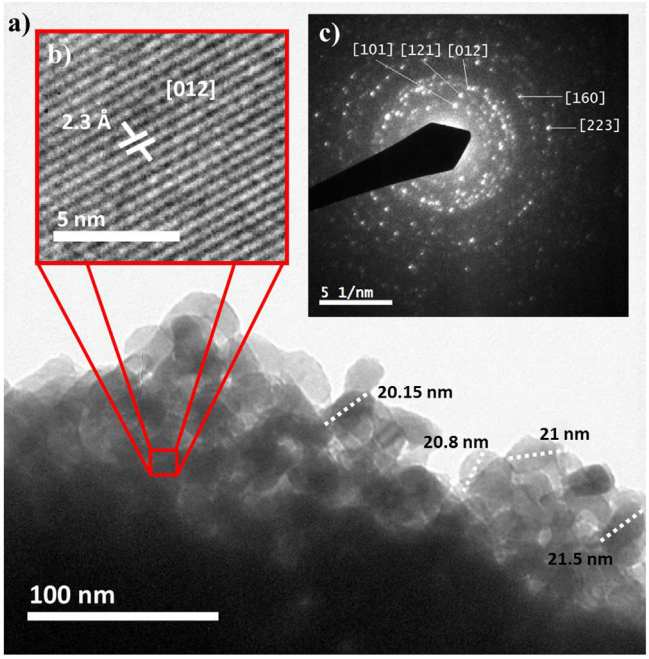


Fig. 2. a) TEM of the Mg_2SiO_4:Er^{3+} 10% nanoparticles presenting a mean diameter of 21 nm. b) Inset presenting the resolved image of the crystal lattice; the Er^{3+} insertion in the host (up to 10%) did not modify the lattice constant. c) ED analysis of the nanoparticles showing several interplanar spacings of crystalline forsterite.

The same elements appear in the EDS measurement (Fig. 3f) of the TEM image (Fig. 3g), in addition to copper and carbon, which originate from the TEM grid used.

High-resolution XPS analyses (Fig. 4) also shows that the insertion of Er^{3+} into the forsterite crystal does not modify it structurally. A comparison of the samples Mg_2SiO_4 (Fig. 4a) and Mg_2SiO_4: Er^{3+}10% (Fig. 4b) show that the Mg 2p, Si 2p and O 1s bands of both samples are very similar. Mg 2p is formed by Mg $2p_{3/2}$ with a center at 50.11 eV and Mg $2p_{1/2}$ at 50.38 eV. The Si 2p band consists of Si $2p_{3/2}$ and Si $2p_{1/2}$ located at 101.80 eV and 102.41eV respectively, while the O 1s band is represented at the 530.8 eV position. The Si 2p and O 1s bands are mainly related to the bonding energies of the tetrahedral conformation with oxygen (SiO^{-4}) [42]. Erbium doping did not alter the behavior of SiO^{-4} in the forsterite structure, as the cation substitution does not affect the oxygen spectrum.

Commercial Er_2O_3 was also analyzed by XPS in order to compare the behavior of Er^{3+} in the forsterite structure and in the oxide form, as well as to evaluate the possible Er_2O_3 formation along with the production of Mg_2SiO_4: Er^{3+} 10%. The Er_2O_3 analyses showed two peaks for the oxygen spectrum (Fig. 4c). The peak at 530.6 eV corresponds to a metal oxide and the peak at 532.8 eV to hydroxide [43]. Erbium oxide is hygroscopic and immediately upon its formation it absorbs moisture and CO_2 from the atmosphere, with both oxide and $Er(OH)_3$ being common in the same product [44]. The oxygen spectrum for Mg_2SiO_4:Er^{3+} 10% clearly does not present the band referring to hydroxide formation, conserving the oxygen configuration in the forsterite structure. The conservation of the forsterite O 1s band configuration without the hydroxide formation is an indication that the erbium present in the sample is shielded inside the structure [43,45,46].

In order to evaluate the non-radiative pathways involved in the decay of excited crystals, an analysis of the E-k dispersion of the matrix would be ideally suited. Nonetheless, a thorough simulation of the Brillouin zone of the material would require precise information on the positioning and interaction of the phosphors inside the supercell, which was not the focus of the present study. Furthermore, the symmetry operations contained in the forsterite unit cell is rather complex even in the absence of the dopant [47]. Nevertheless, Raman spectroscopy is one of the most powerful and trustworthy methods when empirically assessing the phonon density at each frequency in crystals, since it is a direct representation of the number of possible harmonic quasiparticles allowed by the lattice [48]. Albeit this technique only represents vibrational modes that affect the polarizability of the system, the vast majority of phonons in real crystals obey this rule. Raman spectroscopy analyses (Fig. 5) were performed for all samples. The undoped Mg_2SiO_4 sample shows quite a different optical activity from the doped ones, which also present completely different spectra when compared to erbium oxide. Unexpected bands are present in the doped structures (around 120, 160, 405, 450, 473, 925 and 952 cm^{-1}), which are neither related to the Mg_2SiO_4 nor to the Er_2O_3 spectra, suggesting a system with novel optical properties. While for 1% mol doping these bands are still poorly defined, as the erbium concentration increases in the host, the bands become better resolved, becoming well-defined above 7% mol doping.

Fig. 6 shows the absorbance spectra in the UV–Vis–NIR determining the regions where the Mg_2SiO_4: Er^{3+} system absorbs with varying dopant concentrations. Sharp peaks characterize the high degree of crystallinity of the prepared samples. As forsterite does not exhibit optical activity in the analyzed region, the bands presented by the Mg_2SiO_4:Er^{3+} system at all concentrations are directly related to the erbium 4f-4f electronic transitions [49,50]. The absorption intensities vary according to the amount of dopant in the structure; the larger the dopant concentration, the higher the

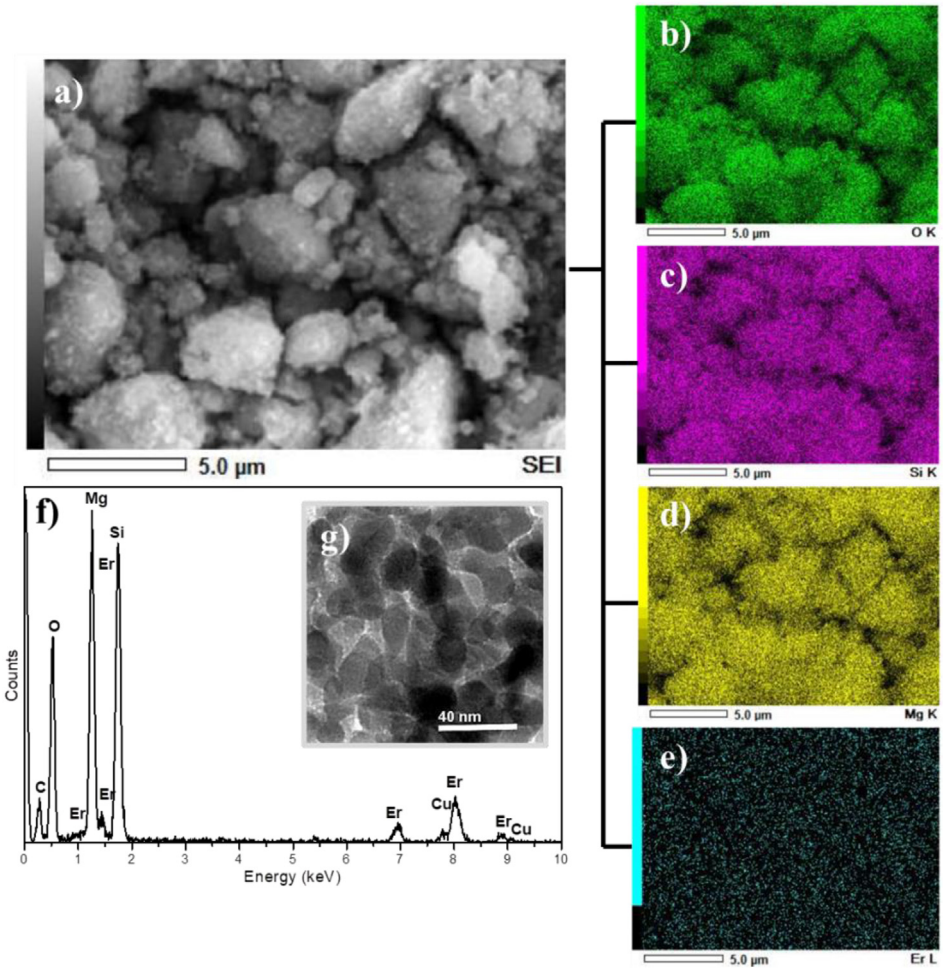


Fig. 3. a) $Mg_2SiO_4:Er^{3+}$ 10% SEM and compositional EDS mapping of b) oxygen c) silicon d) magnesium and e) erbium. f) EDS spectra with its g) receptive TEM image. The EDS mapping shows homogeneous distribution with no clusters of any element. Oxygen, silicon, magnesium and erbium appear in the EDS measurement in addition to copper and carbon from the TEM grid used.

absorption intensity.

In the absorption spectrum, the following peaks were identified in the UV–Vis–NIR region (300–1100 nm): $^4G_{11/2}$ (375 nm), (^2G, ^4F, $^2H)_{9/2}$ (413 nm), $^4F_{5/2}$ (448 nm), $^4F_{7/2}$ (511 nm), $^2H_{11/2}$ (530 nm), $^4S_{3/2}$ (545 nm), $^4F_{9/2}$ (660 nm), $^4I_{9/2}$ (801 nm), $^4S'_{3/2}$ (850 nm) and $^4I_{11/2}$ (980 nm). With the exception of the $^4S'_{3/2}$ level, related to the $^4S_{3/2}$ absorption from the $I_{13/2}$ excited state, all the bands are related to the absorption from the ground state ($^4I_{15/2}$). The discrimination of the optical absorption bands was realized based on previous studies [18,51–55]. As a result of the dopant and the host interaction, the background intensity rises as erbium concentration increases in the forsterite structure [56]. The absorption spectrum of rare earth ions is influenced by the nature of the host structure, due to its pivotal role in the excitation spectrum of the 4f electrons. Their spectra are sensitive to changes in the coordination number, degree of disorder and symmetry of the site that the ions occupy. The wavelength and/or intensity of the bands associated with the absorption spectrum may vary as they depend on the host and dopant concentration [57].

Fig. 7 shows the photoluminescence downconversion spectra of $Mg_2SiO_4:Er^{3+}$ (0–20%) samples under 532 nm excitation. The spectra present the characteristic Er^{3+} emission bands for the crystalline host. Forsterite shows no emission in the analyzed UV–Vis–NIR region, as observed in the Mg_2SiO_4 spectrum. As the dopant concentration in the host is increased, the emission intensity increases accordingly. The $Mg_2SiO_4:Er^{3+}$ system presented emissions at 545 nm, 660 nm, 801 nm and 980 nm, related the radiative relaxation of $^4S_{3/2}$, $^4F_{9/2}$, $^4I_{9/2}$ and $^4I_{11/2}$ states, respectively, to the ground state ($^4I_{15/2}$). The 850 nm emission is related to the $^4S_{3/2} \rightarrow {}^4I_{13/2}$ transition that occurs in parallel with the $^4S_{3/2}$, $^4F_{9/2}$, $^4I_{9/2}$ relaxations to the ground state [58]. The $^4S_{3/2} \rightarrow {}^4I_{13/2}$ transition (850 nm emission) followed by $^4I_{13/2} \rightarrow {}^4I_{15/2}$ (1530 nm emission, presented further below in this section) is very important in the optical communication field [58,59]. The broad band between 545 nm and 900 nm that increases with the dopant concentration, is attributed to the partial overlap of all transitions present in this region [60].

The emission spectra for the different compositions excited at 985 nm can be seen in Fig. 8. A maximum in emission is observed for the $Mg_2SiO_4:Er^{3+}$ 7%. The initial upconversion enhancement with increasing erbium concentration up to 7% mol can be explained by the increasing number of emitting centers, as well as the decreasing number of possible non-radiative decay paths, as depicted in Fig. 5. Raman modes which were active up to 5% Er^{3+} either disappear with increasing concentration or become less broadened at higher chromophore concentrations. The increased number of active phonons, especially at higher wavenumbers as seen in Fig. 5, might help to account for the decrease in fluorescence intensity with reduced erbium concentration. These additional vibrational modes might work towards inducing multiphonon

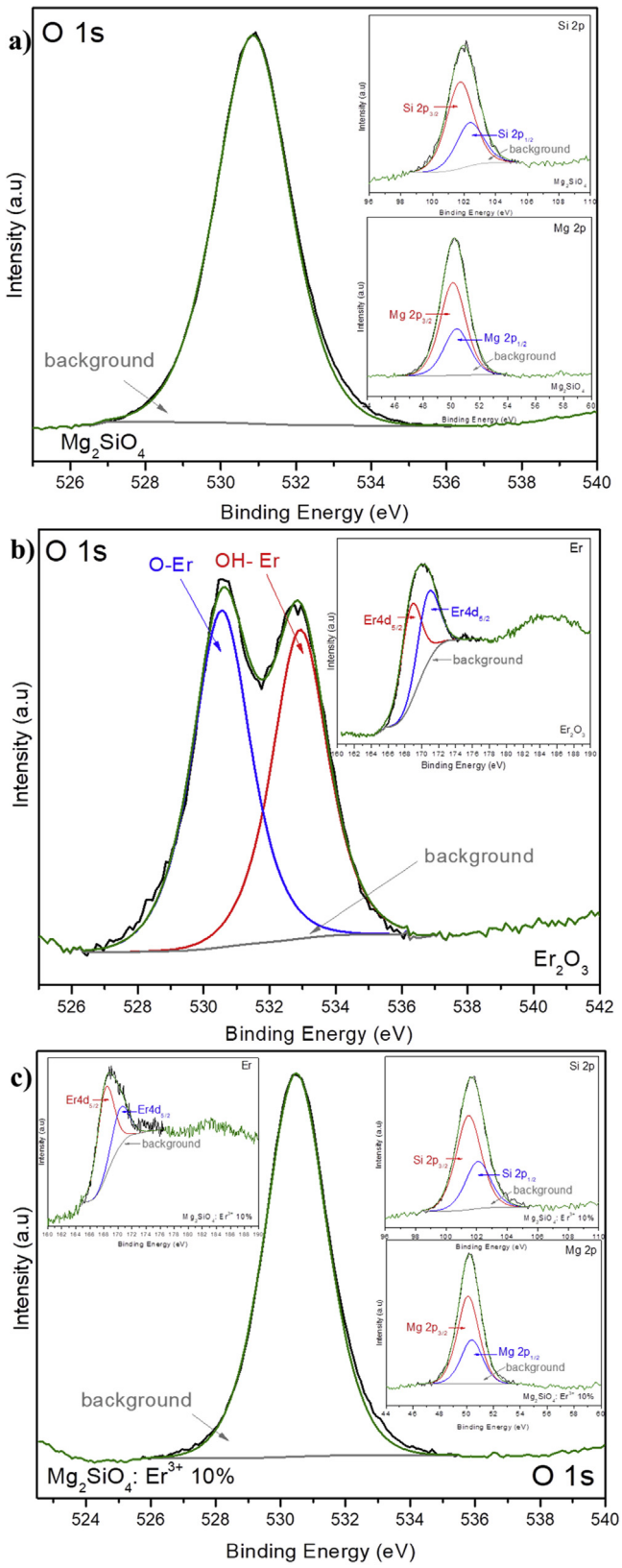


Fig. 4. XPS analyses comparing the high-resolution spectra of the a) Mg_2SiO_4 and b) Mg_2SiO_4:Er^3 10% nanoparticles and c) commercial Er_2O_3. The insertion of Er^{3+} into the forsterite crystal does not modify it structurally.

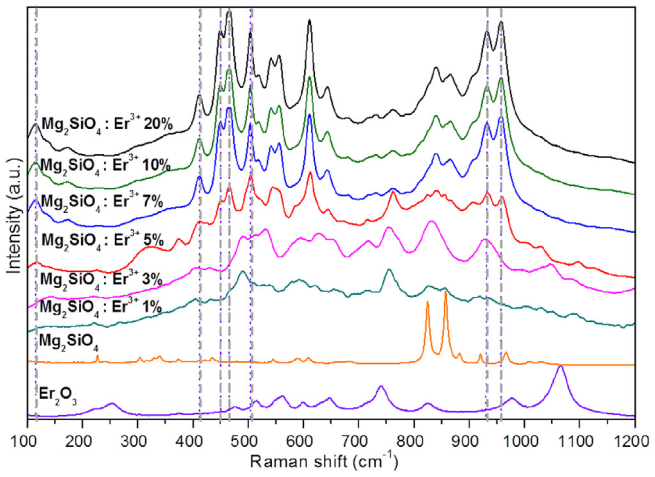


Fig. 5. Raman spectra of Mg_2SiO_4:Er^{+3} (0, 1, 3, 5, 7, 10 and 20%) and Er_2O_3. The undoped Mg_2SiO_4 sample shows quite a different optical activity from the doped ones, which also present completely different spectra when compared to erbium oxide, suggesting a system with novel optical properties to the doped structures.

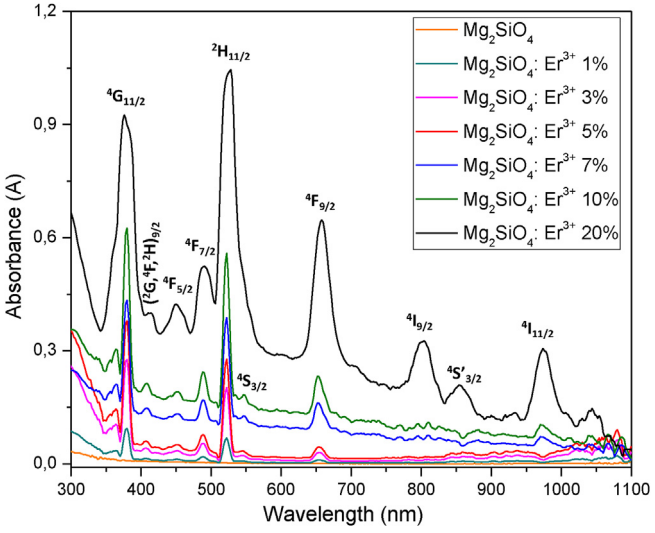


Fig. 6. Absorption spectra of Mg_2SiO_4:Er3+ (0–20%) in the UV–Vis–NIR region. The bands presented by the Mg_2SiO_4:Er^{3+} system at all concentrations are directly related to the erbium 4f-4f electronic transitions.

decay, decreasing the likelihood of radiative emission in the samples with low erbium concentration.

Furthermore, at concentrations above 7% mol, the relative emission also decreases. The same phonons are active at higher amounts of erbium, as shown by their similar Raman spectra, indicating that another mechanism is affecting this decrease. Concentration quenching is the most likely reason; internal emission from excited erbium atoms might further excite lanthanide sites which are allowed non-radiative decay pathways and thus do not contribute to the overall emission yield [61].

Another important aspect from the emission spectra is the relative intensity between green and red fluorescence bands. The relative quantum yield data is summarized in Fig. 9. The green emission, whose band is centered at 550 nm and corresponds to the $^4S_{3/2} \rightarrow {}^4I_{15/2}$ transition, is less intense than the red emission (655 nm, $^4F_{9/2} \rightarrow {}^4I_{15/2}$) for all compositions, except for the sample prepared with 7% of erbium. A linear relation between erbium concentration and quantum yield can be found for the red emission,

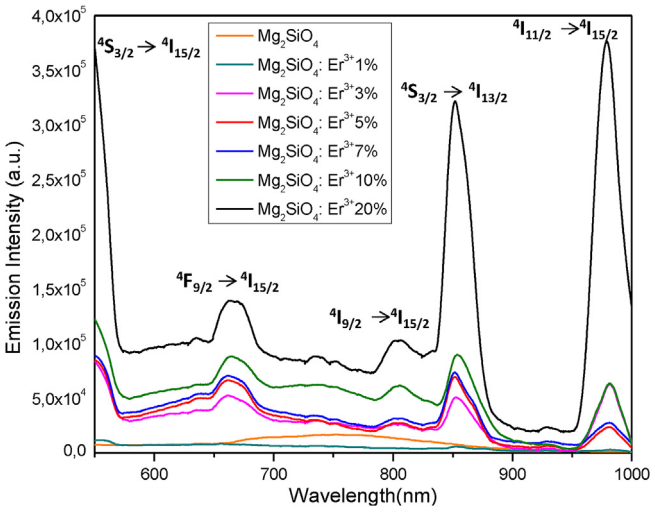


Fig. 7. Photoluminescence downconversion spectra of the produced samples, excited at 532 nm. With the exception of the $^4I_{13/2}$ level, related to the $^4S_{3/2}$ relaxation, all emissions are related to the relaxation to the ground state ($^4I_{15/2}$15/2).

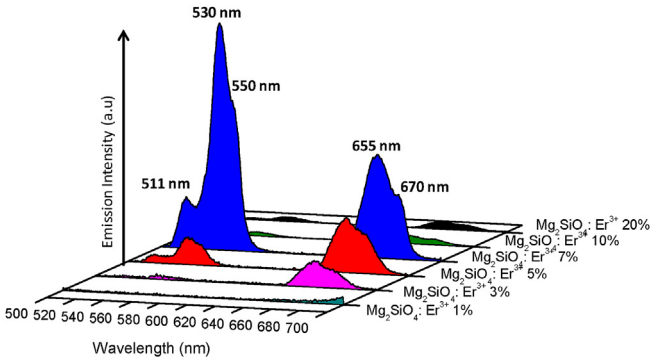


Fig. 8. Photoluminescence upconversion spectra of the produced samples excited at 980 nm. A maximum in emission is observed for the Mg_2SiO_4:Er^{3+} 7%.

whereas the green emission increases at a much faster rate.

The emission spectra for the different compositions excited at 808 nm can be seen in Fig. 10. Interestingly, the emission spectra are vastly different from those observed under 985 nm excitation. When excited with these more energetic photons, only the green emission was measured for all the samples.

Since the same material displays different emissive behavior for different excitation wavelengths, the storage levels which fuel the red emission are not being filled when the system is excited at 808 nm. Two pathways are possible to account for this phenomenon. One of them is based on the fact that the storage levels might be completely independent, i.e. there is no crossing between the emitting states. Therefore, electrons in one level cannot hop to the lower-lying level. Another possibility is that the virtual level excited on upconversion might have an increased probability of decay via non-radiative levels, which would be faster than necessary to populate the levels decaying via red emission. The green levels, on the other hand, have enough time to become populated and exhibit their expected radiative decay. The possible mechanisms giving rise to both emissions when the system is excited at 985 and 808 nm are depicted in Fig. 11.

The dominant upconversion mechanisms in erbium-doped materials have been extensively studied [50,62,63]. There are two main pathways for the excitation, namely excited state absorption

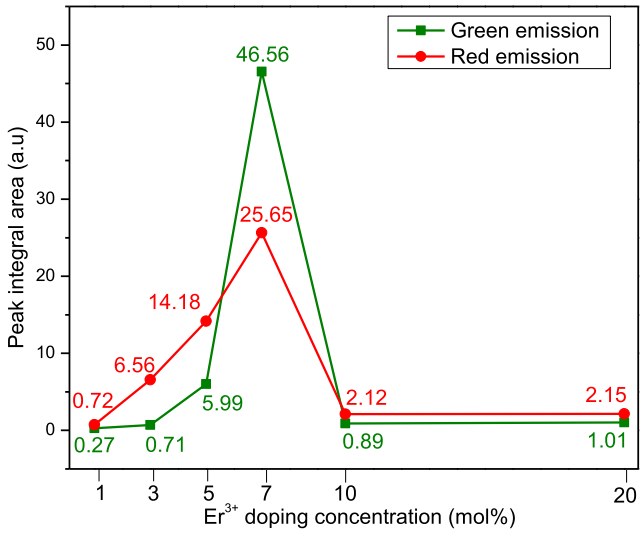


Fig. 9. Comparison between the area of the peaks related to green emission (530 nm) and red emission (660 nm) for all Mg_2SiO_4:Er^{3+} (1–20%) produced samples. A linear relation between erbium concentration and quantum yield can be found for the red emission, whereas the green emission increases at a much faster rate. . (For interpretation of the references to colour in this figure legend, the reader is referred to the Web version of this article.)

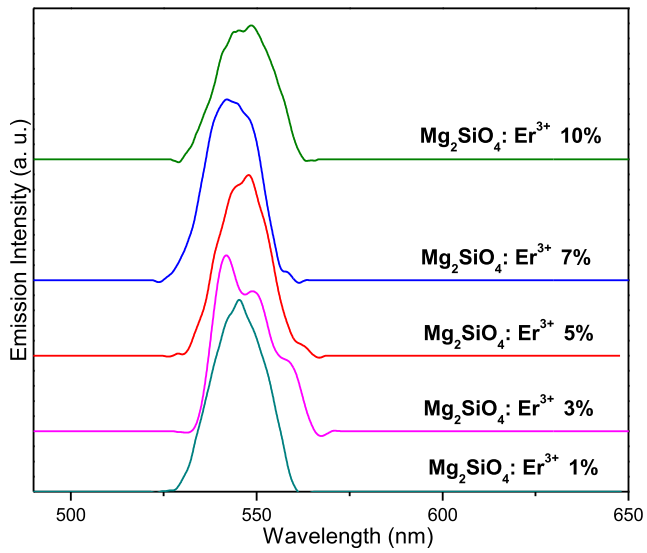


Fig. 10. Photoluminescence upconversion spectra of the produced samples excited at 808 nm. Only the green emission was measured for all the samples. . (For interpretation of the references to colour in this figure legend, the reader is referred to the Web version of this article.)

(ESA) and energy transfer upconversion (ETU). The first involves the absorption of a second photon by a previously excited atom, while the latter implies the energy transfer between two neighboring excited atoms, with one of them decaying in the process. ETU processes usually become relevant at concentrations above 1%; they could therefore be responsible for the observed fluorescence [64].

The initial absorption of a 985 nm photon takes the chromophore to its $^4I_{11/2}$ level. The uptake of a second photon of 985 nm leads the system to the $^4F_{7/2}$ state [65], which usually decays via green fluorescence due to the $^4S_{3/2} \rightarrow {}^4I_{15/2}$ transition [62]. This energy uptake might occur via both ESA and ETU. Nonetheless, the rapid growth in quantum yield with increasing erbium

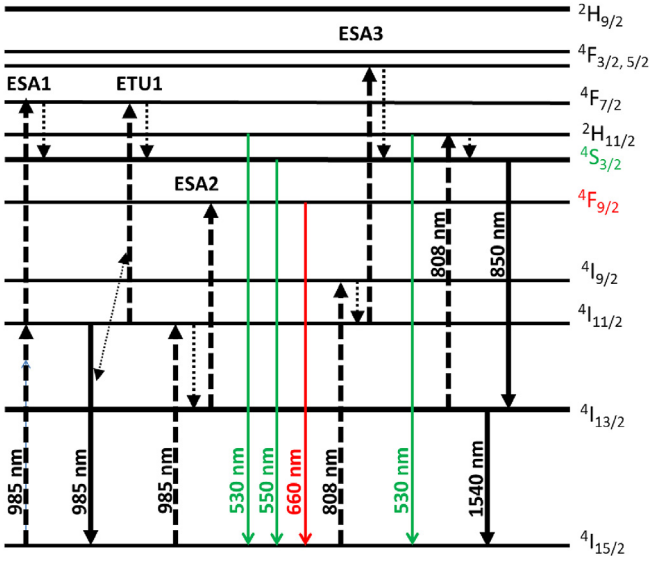


Fig. 11. Schematic energy level diagram showing the possible upconversion processes ESA 1, 2, 3 and ETU 1 for Er^{3+} in the Mg_2SiO_4 host, under 985 nm and 808 nm excitation. The dashed, dotted, and full arrows represent excitation, nonradiative relaxation, and emission processes, respectively.

concentration (Fig. 9) points toward processes involving more than one emitting center. Therefore, it is safe to assume that most of the upconversion leading to the green emission takes place via ETU, since the probability that an excited erbium atom can interact with other nearby excited species grows in a likewise fashion as to that observed for the quantum yields. At lower concentrations, the dopant ions are placed too far apart in order to cooperate towards upconversion, while at higher amounts there is an ever-increasing probability that erbium ions neighbor one another. Upconversion via ESA might also be contributing towards the overall fluorescence, albeit at lower rates. After the transition towards the upper excited state, non-radiative pathways populate the $^2H_{11/2}$ and $^4S_{3/2}$ levels, whence the green emission occurs [66].

On the other hand, the red emission under 985 nm excitation has a linear relation to the erbium amount present in forsterite. The slope of the curve indicates that upconversion is likely to involve a single absorbing center i.e. via ESA. Furthermore, the overall detachment between the growth rates of both emissions reveals a disconnection between the two processes. While multiphonon relaxation (MPR) is energetically allowed between the $^4S_{3/2}$ and $^4F_{9/2}$ states (3 phonons) [67], the increased population of the green state does not translate into equally increased red emission.

The most probable candidate for storage level in ESA is $^4I_{13/2}$. While initially empty according to Boltzmann statistics, this state is quickly filled [68]. The gap between $^4I_{11/2}$ and $^4I_{13/2}$, of approximately 3700 cm^{-1} can easily be bridged via MPR. Furthermore, a parasitic emission in 850 nm – related to the $^4S_{3/2} \rightarrow {}^4I_{13/2}$ transition – quickly pumps electrons towards the latter. Further non-radiative decay from this level is hindered by the large amount of phonons which would be necessary (8 phonons). This strong effect can also be seen in Fig. 6, where the $^4I_{13/2}$ level is so populated that it even contributes to the absorption spectra of the samples. Under the absorption of a second 985 nm photon, a transition to $^4F_{9/2}$ occurs, which thus leads to the emission at 660 nm.

The absence of the red emission under 808 nm excitation further corroborates the idea that the red emission arises from the above mentioned ESA process. In this case the absorption of a second photon from the lowest-lying excited level ($^4I_{13/2}$) would lead the system directly to the $^2H_{11/2}$ state, which decays via green emission. Since no sensible crossing between red and green levels takes place in forsterite, the red emission is efficiently quenched [69].

The proposed ESA mechanisms for the excitation at 985 nm are the following:

$$Er^{3+}(^4I_{15/2}) + h\nu\ (985\ nm) \rightarrow Er^{3+}(^4I_{11/2})$$

$$\text{ESA1: } Er^{3+}(^4I_{11/2}) + h\nu\ (985\ nm) \rightarrow Er^{3+}(^4F_{7/2})$$

$$Er^{3+}(^4F_{7/2}) \rightarrow Er^{3+}(^4H_{11/2}) \rightarrow Er^{3+}(^4I_{15/2}) + h\nu\ (530\ nm)$$

or

$$Er^{3+}(^4F_{7/2}) \rightarrow Er^{3+}(^4S_{3/2}) \rightarrow Er^{3+}(^4I_{15/2}) + h\nu\ (550\ nm)$$

$$Er^{3+}(^4I_{11/2}) \rightarrow Er^{3+}(^4I_{13/2})$$

$$\text{ESA2: } Er^{3+}(^4I_{13/2}) + h\nu\ (985\ nm) \rightarrow Er^{3+}(^4F_{9/2}) \rightarrow Er^{3+}(^4I_{15/2}) + h\nu\ (660\ nm)$$

Upconversion via ETU processes can occur in a multitude of ways, depending on the rate of decay of the $^4I_{11/2}$ state. Disregarding such excited state deactivation:

$$\text{ETU1: } Er^{3+}(^4I_{11/2}) + Er^{3+}(^4I_{11/2}) \rightarrow Er^{3+}(^4I_{15/2}) + Er^{3+}(^4S_{3/2})$$

Conversely, for the excitation at 808 nm, the following mechanism is proposed:

$$Er^{3+}(^4I_{15/2}) + h\nu(808\ nm) \rightarrow Er^{3+}(^4I_{9/2}) \rightarrow Er^{3+}(^4I_{11/2})$$

$$\text{ESA3: } Er^{3+}(^4I_{11/2}) + h\nu\ (808\ nm) \rightarrow Er^{3+}(^4F_{5/2})$$

Once the Er^{3+} substitutional doping might occupy the octahedral sites in the host, the system Mg_2SiO_4:Er^{3+} can be as well represented as $Er_xMg_x(SiO_4)$. To obtain high upconversion luminescence efficiency, the distance between the Er^{3+} ions needs to be very short. Usually, the doping concentration of Er^{3+} ions is very low because of the constraint of solid concentrations in conventional Er^{3+} doped silicon or silica materials (1019 cm^{-3}). Erbium silicates allow high density of Er^{3+} ions (~1022 cm^{-3}), 100 times higher than that of other Er^{3+} doped materials [70].

The NIR emission of erbium-doped forsterite has also been studied. Fig. 12 exhibits the emission spectrum of the samples when excited at 985 nm. The emission displays a very intricate fine structure centered at 1530 nm. Once again, the sample Mg_2SiO_4:Er^{3+}7% presents the most intense emission. The sample Mg_2SiO_4:Er^{3+} 5% also displays a strong NIR emission.

The emission at 1530 nm is well established in the literature as being related to the $^4I_{13/2} \rightarrow {}^4I_{15/2}$ transition. It is worth noting that this transition is of extreme importance in the telecommunications industry [71–74]. The fine structure is explained by the stronger effect of Stark splitting at larger wavelengths. The variation in dopant concentration leads to distinct structural interactions, changing the radiative and non-radiative relaxation paths. The presence of Stark split peaks is very common for crystalline doped structures. Depending on the host:dopant relaxation paths created, these peaks may appear sharp and defined or overlapped as broad peaks [60,64].

The relatively strong emission displayed by all samples further corroborates the hypothesis that the $^4I_{13/2}$ is highly populated. The large number of erbium ions at this level increases the probability of NIR emission. Samples Mg_2SiO_4:Er^{3+} 5% and 7% mol display similar emission from the $^4I_{13/2}$ decay. The latter is much more

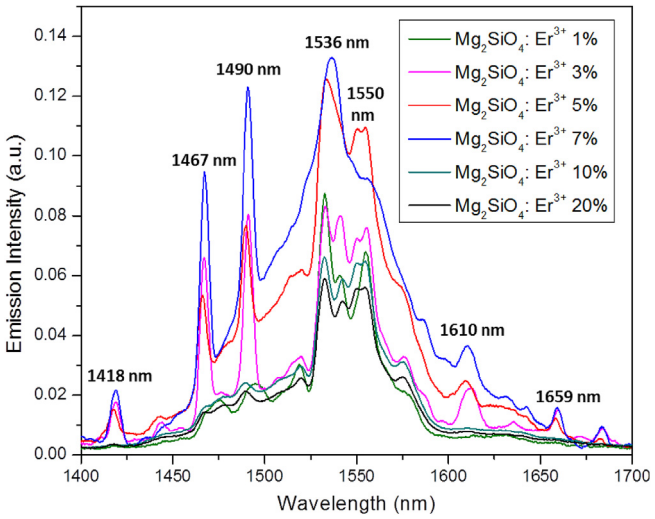


Fig. 12. Photoluminescence downconversion spectra of the produced samples under 985 nm excitation. The emission displays a very intricate fine structure centered at 1530 nm.

fluorescent when analyzed for upconversion, further indicating the importance of the extra Raman modes active in the 5% sample. Although both have similarly populated $^4I_{13/2}$ which would contribute for visible emission, the higher energy and density of phonons in the sample with lower erbium concentration is contributing towards an overall decrease in observed visible fluorescence.

4. Conclusions

In this work, we successfully synthesized erbium-doped forsterite with no secondary phase formation up to 10% mol of dopant concentration by RSC. This exceptional high amount of dopant was possible by substitutional erbium atoms allocating themselves into the forsterite magnesium octahedral sites, without altering the host structure. The nanoparticles produced demonstrate high optical activity with increasing absorption and downconversion proportional to the doping level (from 1 to 20% mol of erbium). Under 985 nm excitation, the sample showed upconversion emission in the red and green range, with a maximum emission at 7% mol of doping as well as surprising inversion of intensities between red and green. However, under 808 nm excitation, all samples showed upcoversion emission only in the green region, with similar intensities. This behavior can be explained by the ESA and ETU process that takes place for the green emission while only the ESA process was proved to be allowed to the red emission in the forsterite structure. Due to the parasitic emission in 850 nm – related to the $^4S_{3/2} \rightarrow {}^4I_{13/2}$ transition, the red emission is observed only with 985 nm excitation, since the excitation at 808 nm in the proposed ESA process leads always to energy levels above $^4S_{3/2}$, resulting in green emission. These results make Mg_2SiO_4:Er^{3+} system a promising candidate as UCNPs for biomedical applications. Its tunable properties allow both treatment and diagnosis by simply changing excitation sources. There is still room for enhancement of its performance such as optimizing the erbium concentration, the use of co-dopants and different functionalization.

Acknowledgements

The authors would like to thank the Coordination for the Improvement of Higher Education Personnel-CAPES for the financial support and the Microscopy and Microanalysis Center of Federal University of Rio Grande do Sul (CMM/UFRGS) for the technical support.

References

[1] G. Bai, M. Tsang, J. Hao, Luminescent ions in advanced composite materials for multifunctional applications, Adv. Funct. Mater. (2016) 6330–6350, https://doi.org/10.1002/adfm.201602142.
[2] B.G. Yust, D.K. Sardar, L.C. Mimun, A.K. Gangadharan, A.T. Tsin, Rare earth doped nanoparticles in organic and inorganic host, nanoscale imaging, Sens. Actuation Biomed. Appl. 8594 (2013) 1–9, https://doi.org/10.1117/12.2004939.
[3] M. Wang, C.-C. Mi, J.-L. Liu, X.-L. Wu, Y.-X. Zhang, W. Hou, F. Li, S.-K. Xu, One-step synthesis and characterization of water-soluble NaYF4:Yb,Er/Polymer nanoparticles with efficient up-conversion fluorescence, J. Alloys Compd. 485 (2009) L24–L27, https://doi.org/10.1016/j.jallcom.2009.05.138.
[4] Y.F. Wang, G.Y. Liu, L.D. Sun, J.W. Xiao, J.C. Zhou, C.H. Yan, W.E.T. Al, Nd 3 þ -Sensitized upconversion Nanophosphors: efficient in vivo bioimaging probes with minimized heating e ff ect, ACS Nano 7 (2013) 7200–7206, https://doi.org/10.1021/nn402601d.
[5] M. Cláudia, A. Issa, M. Manela-Azulay, Photodynamic therapy: a review of the literature and image documentation, An. Bras. Dermatol. 85 (2010) 501–511.
[6] D.F. Dennis, E.J.G.J. Dolmans, R.K. Jain, Photodynamic therapy for cancer, Nat. Rev. Cancer 3 (2003) 380–387, https://doi.org/10.1038/nrc1071.
[7] D. Van Straten, V. Mashayekhi, H.S. De Bruijn, S. Oliveira, D.J. Robinson, Oncologic Photodynamic Therapy: Basic Principles, Current Clinical Status and Future Directions, 2017, pp. 1–54, https://doi.org/10.3390/cancers9020019.
[8] F. Ai, Q. Ju, X. Zhang, X. Chen, F. Wang, G. Zhu, A core-shell-shell nanoplatform upconverting near-infrared light at 808 nm for luminescence imaging and photodynamic therapy of cancer,, Sci. Rep. 5 (2015) 10785, https://doi.org/10.1038/srep10785.
[9] H. Wang, R. Han, L. Yang, J. Shi, Z. Liu, Y. Hu, Y. Wang, S. Liu, Y. Gan, Design and synthesis of core–shell–shell upconversion nanoparticles for NIR-induced drug release, photodynamic therapy, and cell imaging, ACS Appl. Mater. Interfaces 8 (2016) 4416–4423, https://doi.org/10.1021/acsami.5b11197.
[10] X. Liang, J. Fan, Y. Wang, Y. Zhao, R. Jin, T. Sun, M. Cheng, X. Wang, Synthesis of hollow and mesoporous structured NaYF4:Yb,Er upconversion luminescent nanoparticles for targeted drug delivery, J. Rare Earths 35 (2017) 419–429, https://doi.org/10.1016/S1002-0721(17)60929-3.
[11] A.Y. Rwei, W. Wang, D.S. Kohane, Photoresponsive nanoparticles for drug delivery, Nano Today 10 (2015) 451–467, https://doi.org/10.1016/j.nantod.2015.06.004.
[12] R. Han, H. Yi, J. Shi, Z. Liu, H. Wang, Y. Hou, Y. Wang, pH-Responsive drug release and NIR-triggered singlet oxygen generation based on a multifunctional core–shell–shell structure, Phys. Chem. Chem. Phys. 18 (2016) 25497–25503, https://doi.org/10.1039/C6CP05308D.
[13] H. Liu, Y. Fu, Y. Li, Z. Ren, X. Li, G. Han, C. Mao, A fibrous localized drug delivery platform with NIR-triggered and optically monitored drug release, Langmuir 32 (2016) 9083–9090, https://doi.org/10.1021/acs.langmuir.6b02227.
[14] S.O. Poelma, S.S. Oh, S. Helmy, A.S. Knight, G.L. Burnett, H.T. Soh, C.J. Hawker, J. Read de Alaniz, Controlled drug release to cancer cells from modular one-photon visible light-responsive micellar system, Chem. Commun. 52 (2016) 10525–10528, https://doi.org/10.1039/C6CC04127B.
[15] B. Liu, Y. Chen, C. Li, F. He, Z. Hou, S. Huang, H. Zhu, X. Chen, J. Lin, Poly (acrylic acid) modifi cation of Nd 3 + -Sensitized upconversion nanophosphors for highly effi cient UCL imaging and pH-responsive drug delivery, Adv. Funct. Mater. (2015) 4717–4729, https://doi.org/10.1002/adfm.201501582.
[16] R. Weissleder, V. Ntziachristos, Shedding light onto live molecular targets, Nat. Med. 9 (2003) 123–128, https://doi.org/10.1038/nm0103-123.
[17] Y. Liu, Y. Lu, X. Yang, X. Zheng, S. Wen, F. Wang, X. Vidal, J. Zhao, D. Liu, Z. Zhou, C. Ma, J. Zhou, J.A. Piper, P. Xi, D. Jin, Nanoparticles for super-resolution nanoscopy, Nat. Publ. Gr 543 (2017) 229–233, https://doi.org/10.1038/nature21366.
[18] X. Chen, W. Xu, H. Song, C. Chen, H. Xia, Y. Zhu, D. Zhou, S. Cui, Q. Dai, J. Zhang, Highly efficient LiYF4:Yb3+, Er3+ upconversion single crystal under solar cell spectrum excitation and photovoltaic application, ACS Appl. Mater. Interfaces 8 (2016) 9071–9079, https://doi.org/10.1021/acsami.5b12528.
[19] P. Liang, M. Wang, Z. Liu, Synthesis and spectroscopic studies of Zn 4 B 6 O 13 and Eu/Tb single-doped Zn 4 B 6 O 13 phosphors, J. Rare Earths 35 (2017) 441–445, https://doi.org/10.1016/S1002-0721(17)60931-1.
[20] K. Ito, H. Sato, H. Takei, O. Tamada, T. Kitazawa, Synthesis of large high-quality forsterite single crystals to 200 mm length and its significance, Geochem. Geophys. Geosyst. 4 (2003), https://doi.org/10.1029/2001GC000273.
[21] Y. Wu, Y. Ji, J. Xu, J. Liu, Z. Lin, Y. Zhao, Y. Sun, L. Xu, K. Chen, Crystalline phase and morphology controlling to enhance the up-conversion emission from NaYF4:Yb,Er nanocrystals, Acta Mater. 131 (2017) 373–379, https://doi.org/10.1016/j.actamat.2017.04.013.
[22] H. Mao, J.R. Arias-gonzalez, S.B. Smith, I. Tinoco, C. Bustamante, Temperature control methods in a laser tweezers system, Biophys. J. 89 (2005) 1308–1316, https://doi.org/10.1529/biophysj.104.054536.
[23] D.J. Naczynski, M.C. Tan, M. Zevon, B. Wall, J. Kohl, A. Kulesa, S. Chen,

C.M. Roth, R.E. Riman, P.V. Moghe, Rare-earth-doped biological composites as in vivo shortwave infrared reporters, Nat. Commun. 4 (2013) 1–10, https://doi.org/10.1038/ncomms3199.
[24] X. CHAI, J. LI, X. WANG, Y. LI, X. YAO, Color-tunable upconversion photoluminescence and highly performed optical temperature sensing in Er 3 +/Yb 3 + co- doped ZnWO 4, Optic Exp. 22440 (24) (2016) 352–358, https://doi.org/10.1364/OE.24.022438.
[25] Q. Wu, S. Lin, Z. Xie, L. Zhang, Y. Qian, Y. Wang, H. Zhang, Tunable upconversion luminescence of monodisperse Y2O3: Er3+/Yb3+/Tm3+ nanoparticles, Appl. Surf. Sci. (2017), https://doi.org/10.1016/j.apsusc.2017.02.136.
[26] W. Yu, Y. Tian, M. Xing, Y. Fu, H. Zhang, X. Luo, Up-conversion luminescence of NaY(WO4)2: Yb, Er under 1550 and 980 nm excitation, Mater. Res. Bull. 80 (2016) 223–229, https://doi.org/10.1016/j.materresbull.2016.03.013.
[27] N.U. Wetter, A.M. Deana, I.M. Ranieri, L. Gomes, S.L. Baldochi, Influence of excited-state-energy upconversion on pulse shape in quasi-continuous-wave diode-pumped Er: LiYF 4 lasers 46 (2010) 99–104, https://doi.org/10.1109/JQE.2009.2028305.
[28] B.G. Yust, D.K. Sardar, L.C. Mimun, A.K. Gangadharan, A.T. Tsin, in: A.N. Cartwright, D.V. Nicolau (Eds.), Rare Earth Doped Nanoparticles in Imaging and PDT, 2013, p. 85940, https://doi.org/10.1117/12.2004939.
[29] R.T. Cygan, A.C. Lasaga, Dielectric and polarization behavior of forsterite at elevated temperatures, Am. Mineral. 71 (1986) 758–766.
[30] M. Saqaei, M. Fathi, H. Edris, V. Mortazavi, Preparation and biocompatibility evaluation of bioactive glass − forsterite nanocomposite powder for oral bone defects treatment applications, Mater. Sci. Eng. C 56 (2015) 409–416, https://doi.org/10.1016/j.msec.2015.07.002.
[31] O.F.P. Olivine, Dielectric and mechanical properties of plasma-sprayed olivine, Rom. Rep. Phys. 67 (2015) 600–616.
[32] O.S. Pokrovsky, J. Schott, Kinetics and mechanism of forsterite dissolution at 25°C and pH from 1 to 12, Geochem. Cosmochim. Acta 64 (2000) 3313–3325, https://doi.org/10.1016/S0016-7037(00)00434-8.
[33] D. Burnat, M. Schlupp, A. Wichser, B. Lothenbach, M. Gorbar, A. Züttel, U.F. Vogt, Composite membranes for alkaline electrolysis based on polysulfone and mineral fillers, J. Power Sources 291 (2015) 163–172, https://doi.org/10.1016/j.jpowsour.2015.04.066.
[34] Y. Phosphors, Y. Wang, Near-infrared Downconversion in LuPO4: Near-infrared Downconversion, 2016, https://doi.org/10.1166/jnn.2016.11828.
[35] S. Chen, J. Fan, L. Pan, B. Jiang, X. Mao, R. Li, X. Yuan, X. Jiang, L. Zhang, Synthesis of Yb:Lu3Al5O12 nano powders with the reverse strike co-precipitation method: influence of decomposition of NH_4HCO_3, J. Rare Earths 34 (2016) 901–907, https://doi.org/10.1016/S1002-0721(16)60113-8.
[36] R. Zampiva, L. Acauan, L. Dos Santos, R. Castro, A. Alves, C. Bergmann, Nanoscale synthesis of single-phase forsterite by reverse strike co- precipitation and its high optical and mechanical properties, Ceram. Int. (2017), https://doi.org/10.1016/j.ceramint.2017.08.201.
[37] S.A. Bakar, G. Byzynski, C. Ribeiro, Synergistic effect on the photocatalytic activity of N-doped TiO2 nanorods synthesised by novel route with exposed (110) facet, J. Alloys Compd. 666 (2016) 38–49, https://doi.org/10.1016/j.jallcom.2016.01.112.
[38] B.D. Yuhas, D.O. Zitoun, P.J. Pauzauskie, R. He, P. Yang, Transition-metal doped zinc oxide nanowires, Angew. Chem. Int. Ed. 45 (2006) 420–423, https://doi.org/10.1002/anie.200503172.
[39] R.D. Shannon, Revised effective ionic radii and systematic studies of interatomic distances in halides and chalcogenides, Acta Crystallogr. A 32 (1976) 751–767, https://doi.org/10.1107/S0567739476001551.
[40] R.D. Shannon, C.T. Prewitt, Effective ionic radii in oxides and fluorides, Acta Crystallogr. B Struct. Crystallogr. Cryst. Chem. 25 (1969) 925–946, https://doi.org/10.1107/S0567740869003220.
[41] J. Rafferty, Minerals, Britannica, New York, 2012.
[42] V.P. Zakaznova-Herzog, H.W. Nesbitt, G.M. Bancroft, J.S. Tse, X. Gao, W. Skinner, High-resolution valence-band XPS spectra of the nonconductors quartz and olivine, Phys. Rev. B Condens. Matter 72 (2005) 1–13, https://doi.org/10.1103/PhysRevB.72.205113.
[43] G.T.K. Swami, F.E. Stageberg, A.M. Goldman, XPS characterization of erbium sesquioxide and erbium hydroxide, J. Vac. Sci. Technol. A Vacuum, Surfaces, Film 2 (1984) 767–770, https://doi.org/10.1116/1.572568.
[44] A. Siokou, S. Kennou, S. Ladas, An Xps and wf study of the Er/Si(100) interface formation, Surf. Sci. 333 (1995) 580–584.
[45] R. Tholkappiyan, K. Vishista, Combustion synthesis of Mg-Er ferrite nanoparticles: cation distribution and structural, optical, and magnetic properties, Mater. Sci. Semicond. Process. 40 (2015) 631–642, https://doi.org/10.1016/j.mssp.2015.06.076.
[46] T.-M. Pan, C.-H. Lu, Forming-free resistive switching behavior in Nd2O3, Dy2O3, and Er2O 3 films fabricated in full room temperature, Appl. Phys. Lett. 99 (2011), 113509, https://doi.org/10.1063/1.3638490.
[47] K.R. Rao, S.L. Chaplot, N. Choudhury, S. Ghose, J.M. Hastings, L.M. Corliss, D.L. Price, Lattice dynamics and inelastic neutron scattering from forsterite, Mg2SiO4: phonon dispersion relation, density of states and specific heat, Phys. Chem. Miner. 16 (1988) 83–97, https://doi.org/10.1007/BF00201334.
[48] F.S. Gittleson, K.P.C. Yao, D.G. Kwabi, S.Y. Sayed, W.H. Ryu, Y. Shao-Horn, A.D. Taylor, Raman spectroscopy in lithium-oxygen battery systems, ChemElectroChem. 2 (2015) 1446–1457, https://doi.org/10.1002/celc.201500218.
[49] M. Miritello, P. Cardile, R. Lo Savio, F. Priolo, Energy transfer and enhanced 1.54 $μ$m emission in Erbium-Ytterbium disilicate thin films, Opt. Express 19 (2011) 20761–20772, https://doi.org/10.1364/OE.19.020761.
[50] K. Vu, S. Farahani, S. Madden, 980nm pumped erbium doped tellurium oxide planar rib waveguide laser and amplifier with gain in S, C and L band, Opt. Express 23 (2015) 747, https://doi.org/10.1364/OE.23.000747.
[51] L.R.P. Kassab, F.A. Bomfim, J.R. Martinelli, N.U. Wetter, J.J. Neto, C.B. De Araújo, Energy transfer and frequency upconversion in Yb3+-Er 3+-doped PbO-GeO2 glass containing silver nanoparticles, Appl. Phys. B Lasers Opt 94 (2009) 239–242, https://doi.org/10.1007/s00340-008-3249-2.
[52] A.J. Garcia-adeva, Infrared-to-visible upconversion of Er, Transition 21 (2004) 744–752.
[53] Y. Fu, H. Krzyzanowska, K. Ni, J. LaRose, M. Huang, P.M. Fauchet, Strong Er emission from Er doped SiO2/nc-Si multilayers, IEEE Int. Conf. Gr. IV Photon. GFP (2010) 305–307, https://doi.org/10.1109/GROUP4.2010.5643344.
[54] A. Naji, B. Hamida, Review of erbium-doped fiber amplifier, Int. J. Phys. Sci. 6 (2011) 4674–4689, https://doi.org/10.5897/IJPS11.782.
[55] F. Gourbilleau, P. Choppinet, C. Dufour, M. Levalois, R. Madelon, C. Sada, G. Battaglin, R. Rizk, Er emission from Er-doped Si-rich silicon oxide layers synthesised by hydrogen reactive magnetron co-sputtering, Phys. E Low-Dimens. Syst. Nanostruct. 16 (2003) 341–346, https://doi.org/10.1016/S1386-9477(02)00688-4.
[56] Y.H. Peng, G.F. Huang, W.Q. Huang, Visible-light absorption and photocatalytic activity of Cr-doped TiO 2 nanocrystal films, Adv. Powder Technol. 23 (2012) 8–12, https://doi.org/10.1016/j.apt.2010.11.006.
[57] V. Naresh, S. Buddhudu, Analysis of visible-NIR emission and photoluminescence quenching in Er3+:Bi2O3–AlF3–TeO2–B2O3 glasses, Phys. Chem. Glas. Eur. J. Glas. Sci. Technol. Part B 56 (2015) 255–262, https://doi.org/10.13036/17533562.56.5.255.
[58] O. Toma, S. Georgescu, 850 nm emission in Er: YLiF4 upconversion lasers, Rom. J. Phys. 55 (2010) 790–799.
[59] F. Kaczmarek, J. Karolczak, Infrared-to-visible upconversion in erbium fluoride (ZBLAN: Er3+) optical fiber: competition between the parasitic 850-nm fluorescence and the green laser emission at 544 nm, Opto-Electron. Rev. 12 (2004) 247–248.
[60] Z. Liu, J. Bian, Y. Huang, T. Xu, X. Wang, S. Dai, Fabrication and characterization of mid-infrared emission of Pr 3+ doped selenide chalcogenide glasses and fibres, RSC Adv. 7 (2017) 41520–41526, https://doi.org/10.1039/C7RA05319C.
[61] E. Snoeks, P.G. Kik, A. Polman, Concentration quenching in erbium implanted alkali silicate glasses, Opt. Mater. (Amst) 5 (1996) 159–167.
[62] T. Som, B. Karmakar, Efficient green and red fluorescence upconversion in erbium doped new low phonon antimony glasses, Opt. Mater. (Amst) 31 (2009) 609–618, https://doi.org/10.1016/j.optmat.2008.06.018.
[63] J.H. Oh, B.K. Moon, B.C. Choi, J.H. Jeong, J.H. Kim, H.S. Lee, The green upconversion emission mechanism investigation of GdVO4:Yb3+, Er3+ via tuning of the sensitizer concentration, Solid State Sci. 42 (2015) 1–5, https://doi.org/10.1016/j.solidstatesciences.2015.02.010.
[64] Z. Pan, A. Ueda, R. Mu, S.H. Morgan, Upconversion luminescence in Er3+-doped germanate-oxyfluoride and tellurium-germanate-oxyfluoride transparent glass-ceramics, J. Lumin. 126 (2007) 251–256, https://doi.org/10.1016/j.jlumin.2006.07.021.
[65] K. Smits, A. Sarakovskis, L. Grigorjeva, D. Millers, J. Grabis, The role of Nb in intensity increase of Er ion upconversion luminescence in zirconia, J. Appl. Phys. 115 (2014), 213520, https://doi.org/10.1063/1.4882262.
[66] A. Sarakovskis, G. Krieke, Upconversion luminescence in erbium doped transparent oxyfluoride glass ceramics containing hexagonal NaYF4 nanocrystals, J. Eur. Ceram. Soc. 35 (2015) 3665–3671, https://doi.org/10.1016/j.jeurceramsoc.2015.06.014.
[67] T. Som, B. Karmakar, Green and red fluorescence upconversion in neodymium-doped low phonon antimony glasses, J. Alloys Compd. 476 (2009) 383–389, https://doi.org/10.1016/j.jallcom.2008.09.006.
[68] T.J. Whitley, C.A. Millar, R. Wyatt, M.C. Brierley, D. Szebesta, Upconversion pumped green lasing in erbium doped fluorozirconate fibre, Electron. Lett. 27 (1991) 1785, https://doi.org/10.1049/el:19911110.
[69] Q. Pan, D. Yang, S. Kang, J. Qiu, G. Dong, Regulating mid-infrared to visible fluorescence in monodispersed nanocrystals by phase modulation, Nat. Publ. Gr (2016) 1–12, https://doi.org/10.1038/srep37141.
[70] R. Ye, C. Xu, X. Wang, J. Cui, Z. Zhou, Room-temperature near-infrared upconversion lasing in single- crystal Er-Y chloride silicate nanowires, Nat. Publ. Gr (2016) 1–6, https://doi.org/10.1038/srep34407.
[71] X. Liao, X. Jiang, Q. Yang, L. Wang, D. Chen, Spectral properties of Er/Tm co-doped ZBLAN glasses and fibers, Materials (Basel) 10 (2017) 1–9, https://doi.org/10.3390/ma10050486.
[72] Z.M. Sathi, J. Zhang, Y. Luo, J. Canning, G.D. Peng, Improving broadband emission within Bi/Er doped silicate fibres with Yb co-doping, Opt. Mater. Express 5 (2015) 2096, https://doi.org/10.1364/OME.5.002096.
[73] A.M. Markom, M.C. Paul, A. Dhar, S. Das, M. Pal, S.K. Bhadra, K. Dimyati, M. Yasin, S.W. Harun, Performance comparison of enhanced Erbium–Zirconia–Yttria–Aluminum co-doped conventional erbium-doped fiber amplifiers, Opt. - Int. J. Light Electron Opt. 132 (2017) 75–79, https://doi.org/10.1016/j.ijleo.2016.12.041.
[74] L. Bigot, G. Le Cocq, Y. Quiquempois, Few-mode erbium-doped fiber amplifiers: a review, J. Light. Technol 33 (2015) 588–596, https://doi.org/10.1109/JLT.2014.2376975.